Journal of Computational Physics 229 (2010) 5465–5485

Contents lists available at ScienceDirect

Journal of Computational Physics

journal homepage: www.elsevier.com/locate/jcp

High-order parabolic beam approximation for aero-optics

Michael D. White *

Ohio Aerospace Institute, Wright-Patterson Air Force Base, OH 45433-7512, United States

ARTICLE INFO

Article history:
Received 4 May 2009
Received in revised form 12 March 2010
Accepted 29 March 2010
Available online 10 April 2010

Keywords:
Compact difference scheme
Aero-optics
Parabolic beam equation
OPD
Computational error
LES

ABSTRACT

The parabolic beam equations are solved using high-order compact differences for the Laplacians and Runge–Kutta integration along the beam path. The solution method is verified by comparison to analytical solutions for apertured beams and both constant and complex index of refraction. An adaptive 4th-order Runge–Kutta using an embedded 2nd-order method is presented that has demonstrated itself to be very robust. For apertured beams, the results show that the method fails to capture near aperture effects due to a violation of the paraxial approximation in that region. Initial results indicate that the problem appears to be correctable by successive approximations. A preliminary assessment of the effect of turbulent scales is undertaken using high-order Lagrangian interpolation. The results show that while high fidelity methods are necessary to accurately capture the large scale flow structure, the method may not require the same level of fidelity in sampling the density for the index of refraction. The solution is used to calculate a phase difference that is directly compared with that commonly calculated via the optical path difference. Propagation through a supersonic boundary layer shows that for longer wavelengths, the traditional method to calculate the optical path is less accurate than for shorter wavelengths. While unlikely to supplant more traditional methods for most aero-optics applications, the current method can be used to give a quantitative assessment of the other methods as well as being amenable to the addition of more physics.

1. Introduction

Work in the field of laser beam propagation dates back to the 1960s. Traditionally interest was in propagation over large distances in the atmosphere, where variations in the index of refraction are typically dealt with statistically [1]. Recently there has been renewed interest in the near field laser propagation, with a special interest in turrets on airborne platforms. The majority of research in this field has focused on geometrical optical approximations [2,3]. An alternative method is to use the paraxial beam method (also called the parabolic equation or quasi-optical approximation [1]) to solve for the laser propagation. Early work in solving the parabolic equation utilized second order finite-differences in space and either Leapfrog, Crank-Nicolson or alternating direction implicit (ADI) along the beam path [1,4]. For improved accuracy, Fast Fourier Transforms (FFTs) are often used in the transverse direction and the split-step method for advancing the solution along the beam path [5]. Recently, this latter technique combined with a 4th-order Runge–Kutta has been effectively used to study the propagation of short laser pulses [6]. The present work studies the possibility of utilizing high-order compact finite-differences for the transverse derivatives coupled with a Runge–Kutta time integrator for aero-optics problems. As a simplified test case, the propagation of the beam through an idealized density field is considered. It will be shown that the density does not have to have as high a resolution as is needed for beam propagation. This is consistent with other investigations into the subject [7].

* Tel.: +1 937 904 4029.
E-mail address: Michael.White@wpafb.af.mil

0021-9991/$ - see front matter © 2010 Elsevier Inc. All rights reserved.
doi:10.1016/j.jcp.2010.03.046

Nomenclature

A	amplitude of beam envelope
G	Green's function
K_{gd}	Gladstone–Dale constant
Ma	Mach number
R	radius in spherical coordinates
Re_{δ_0}	Reynolds number based on reference boundary layer height
$\mathcal{T}$	Runge–Kutta truncation error
U	scalar representation of beam
a	radius of circular aperture
c_0	speed of light in vacuum
f	focal length of beam
i	$\sqrt{-1}$
k	wavenumber
n	index of refraction
p	power for adaptive Runge–Kutta coefficient
r, θ, z	cylindrical coordinates
r_0	Gaussian $1/e$ radius
x, y, z, t	Cartesian coordinates and time
δ	mean boundary layer height
ϕ	combined Green's function
ψ, $\delta\psi$	phase, phase difference
λ	wavelength of beam
ρ	density
ω	time harmonic frequency

One of the advantages of the current method over the traditional methodologies based on OPD is that it contains more physics. While it is not considered necessary to replace the traditional methods for routine computations, the current approach can be used to help give a quantitative assessment of the accuracy of the methods, as well as being amenable to the addition of more physical modeling, including non-linear effects and beam/flow interaction, should the need arise.

2. Theoretical development

For continuous wave laser propagation with a time harmonic dependence of $e^{-i\omega t}$, Maxwell's Equations can be reduced to the scalar Helmholtz equation [1,4,8,9]:

$$\nabla^2 U + \left(\frac{\omega^2 n^2}{c_0^2}\right) U = 0, \tag{1}$$

where n is the index of refraction, c_0 is the speed of light in vacuum and U is either of the electric filed components perpendicular to the direction of propagation. The frequency is related to the laser wavelength by $\omega = 2\pi c_0/\lambda$, while the index of refraction is related to the density empirically using the Gladstone–Dale constant:

$$n \approx 1 + K_{gd}\rho. \tag{2}$$

The Gladstone–Dale constant for air is approximately (in m^3/kg) [1,10]:

$$K_{gd} \approx 2.24 \times 10^{-4}\left(1 + \frac{7.52 \times 10^{-3}}{\lambda^2}\right)\left[\frac{m^3}{kg}\right] \tag{3}$$

with λ is measured in microns.

For the parabolic equation, the beam is expanded as:

$$U = A(x, y, z)e^{ikz} \tag{4}$$

which results in the equation for propagation of the beam envelop being:

$$\nabla_\perp^2 A + \frac{\partial^2 A}{\partial z^2} + 2ik\frac{\partial A}{\partial z} + k^2\left(\frac{n^2}{n_r^2} - 1\right)A = 0, \tag{5}$$

where $\nabla_\perp$ is the transverse component of the Laplacian. A Schrödinger like equation for the amplitude is obtained by making the paraxial approximation $|\partial_{zz}A| \ll |k\partial_z A|$.

$$\nabla_{\perp}^2 A + 2ik\frac{\partial A}{\partial z} + k^2\left(\frac{n^2}{n_r^2} - 1\right)A \approx 0. \tag{6}$$

Eq. (6) can be generalized to include extra polarization term on the right hand side which can incorporate non-linear effects into the formulation [6].

3. Computational methodology

For the current implementation of the parabolic beam equation, the differences in the transverse plane are computed using high-order compact differencing. Compact finite-differences are derived by using information about the derivatives of neighboring points to increase the accuracy. For instance, the second derivative in x is given as:

$$a_0\left.\frac{\partial^2 A}{\partial x^2}\right|_{j+1,\kappa} + \left.\frac{\partial^2 A}{\partial x^2}\right|_{j,\kappa} + a_0\left.\frac{\partial^2 A}{\partial x^2}\right|_{j-1,\kappa} = a_1\left(\frac{A_{j+1,\kappa} - 2A_{j,\kappa} + A_{j-1,\kappa}}{\Delta x^2}\right) + a_2\left(\frac{A_{j+2,\kappa} - 2A_{j,\kappa} + A_{j-2,\kappa}}{4\Delta x^2}\right) + a_3\left(\frac{A_{j+3,\kappa} - 2A_{j,\kappa} + A_{j-3,\kappa}}{9\Delta x^2}\right), \tag{7}$$

where the coefficients are determined by matching the leading truncation terms of the Taylor series. A similar formulation is given for the derivatives in the y-direction. Coefficients for a_0, a_1, a_2, a_3 are given in Table 1. A nice summary of these methods is given by Lele [11].

The characteristic eigenvalues for the beam Eq. (6) lie entirely on the imaginary axis. Due to the small wavelength, an explicit Runge–Kutta (RK) may be used to integrate the envelope along the beam path. The beam Eq. (6) is discretized as a grid of ordinary differential equations in the $\hat{\mathbf{z}}$-direction coupled in the transverse direction by the Laplacian solved using compact differences:

$$\partial_z A = f(z, A), \tag{8}$$

where

$$f(z, A) = \frac{i}{2k}\nabla_{\perp}^2 A + \frac{ik}{2}\left(\left(\frac{n}{n_r}\right)^2 - 1\right)A. \tag{9}$$

The details of the adaptive Runge–Kutta may be found in Appendix A.

4. Verification of methodology

For verification purposes, the Method of Manufactured Solutions [12] is utilized. To implement this the varying index of refraction in (6) is replaced by:

$$n = n_r\sqrt{\left(1 + \frac{\eta}{k^2}\right)}, \tag{10}$$

where η is a complex function as outlined in Appendix B.

Fig. 1 shows the magnitude of the pulse after propagating to $z = 100$. The error through the center of the beam as it propagates its entire length is shown in Fig. 2. This case was run with the Laplacian being calculated from 2nd to 8th order accuracy using the coefficients in Table 1. The L_1 error at the ending plane was calculated and shown in Fig. 3. If one ignores the points corresponding to the coarsest grid, the slopes are all close to the theoretical. It is interesting to note that the 6th and 8th order cases still retain these slopes when the problem is being marched by a method that is only 4th order in z. However, it should be remembered that the condition to derive the governing equation was that $|\partial_{zz}A| \ll |k\partial_z A|$, and that since the method is explicit, the stability from the Laplacian term will tend to force $\Delta z \propto \lambda/(1/\Delta x^2 + 1/\Delta y^2)$. Further details regarding the effect of the adaptive Runge–Kutta on the error can be found in Appendix A.

Table 1
Coefficients for compact-differencing.

Order	a_0	a_1	a_2	a_3
2	0	1	0	0
4	$\frac{1}{10}$	$\frac{6}{5}$	0	0
6	$\frac{2}{11}$	$\frac{12}{11}$	$\frac{3}{11}$	0
8	$\frac{9}{38}$	$\frac{147}{152}$	$\frac{51}{95}$	$-\frac{23}{760}$

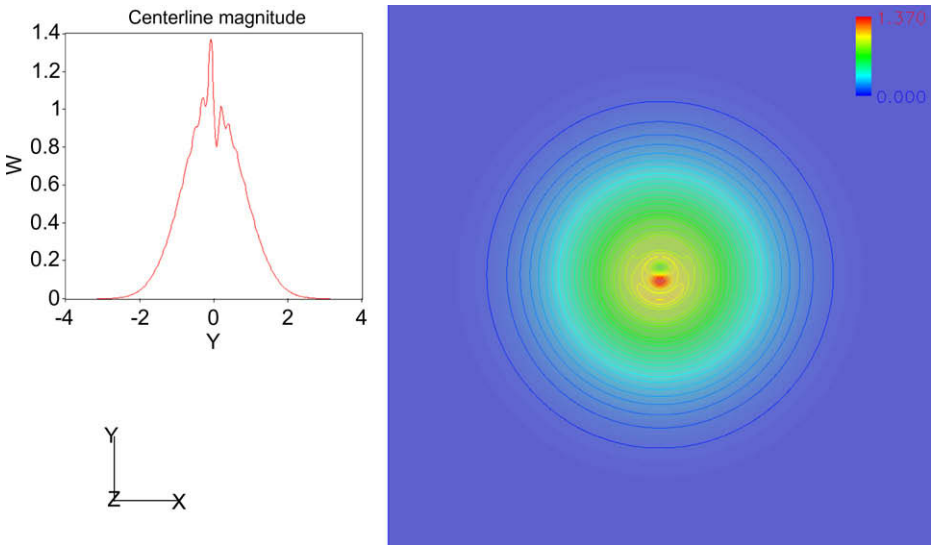

Fig. 1. Amplitude of Gaussian pulse propagated complex index of refraction at $z = 100$ [cf. Eq. (53), Appendix B].

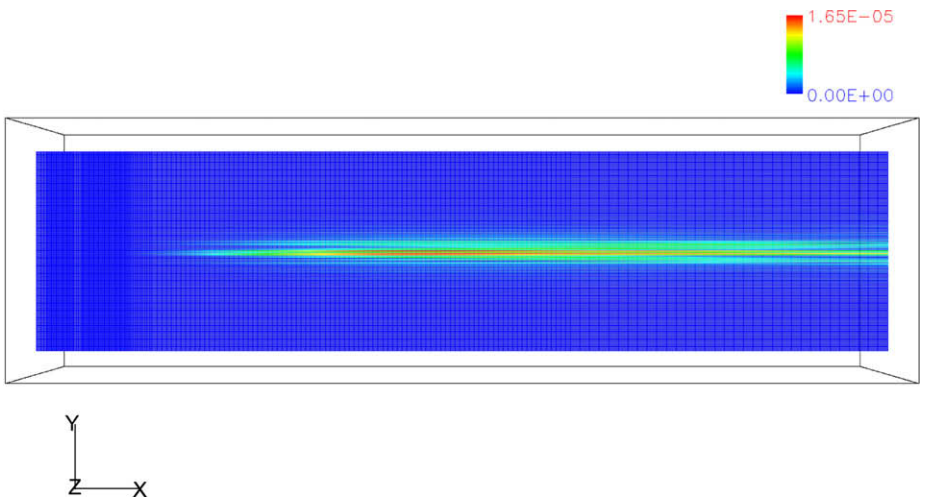

Fig. 2. Error from propagation through complex index of refraction.

5. Computational results and discussion

Fig. 4 shows a Gaussian beam with a target focus at $f = 20$ propagating to $z = 40$. The actual minimum beam waist is just short of f and may be calculated [1]:

$$z_w = \frac{k^2 r_0^4 f}{k^2 r_0^4 + 4f^2}. \tag{11}$$

Once passing the actual focal point, the beam diverges. The symmetry of the solution is apparent; and by taking the complex conjugate of the equations, the beam may be marched in $\pm z$. Only two types of beams are considered in the present work. The first has a Gaussian profile at $z = 0$ of:

$$A = e^{-\left(1+\frac{ikr_0^2}{2f}\right)\left(\frac{r}{r_0}\right)^2}, \tag{12}$$

where the $1/e$ point of the real part is at $r_0 = 1.18$ and $f = 2000$. The second type of beam is a "top-hat" profile modeled by:

$$A = \frac{1 - \tanh\left[s(r - \pi/1.5)\right]}{2}, \tag{13}$$

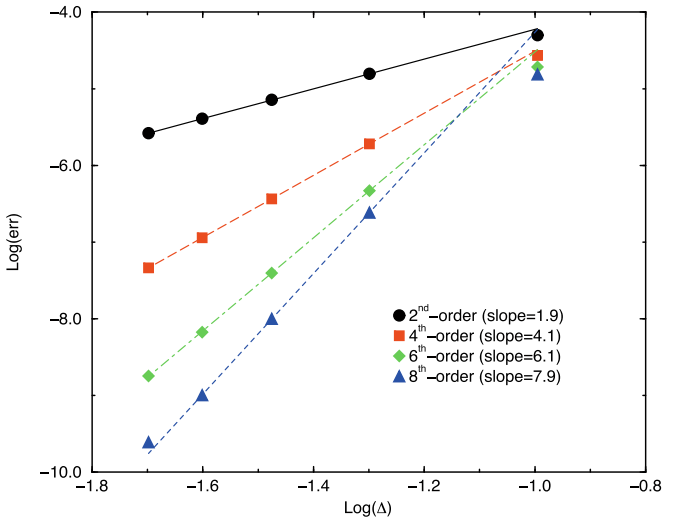

Fig. 3. Grid refinement in transverse direction. [*Note*: rightmost points not included in slope calculation.]

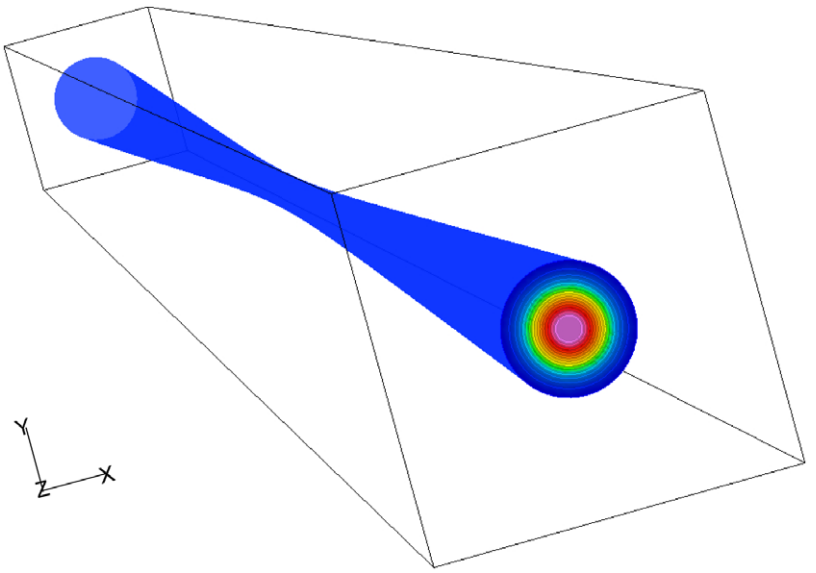

Fig. 4. Gaussian beam with focal length ≈20 propagating in constant density.

where s is the slope of the tangent function. This "top-hat" profile corresponds to $f \to \infty$ and is a purely diverging beam. The computational domain will typically be either $\pm\pi$ or ± 5 in the x–y plane.

5.1. Diffraction effects with constant index of refraction

For constant index of refraction, the Helmholtz equation (1) is typically solved by using Green's Theorem [8,9,13]. If one assumes planar apertures, the inconsistencies of the Fresnel–Kirchhoff diffraction formula can be eliminated by using two Green's functions, so that the function itself vanishes in the aperture [8,9]. The Green's function appropriate for this problem is well known to be [8,13]:

$$G^{\pm}(\mathbf{x},\mathbf{x}') = \frac{e^{ikR^{\pm}}}{4\pi R^{\pm}}, \tag{14}$$

where

$$R^{\pm} = \sqrt{(x-x')^2 + (y-y')^2 + (z \mp z')^2} \tag{15}$$

and the wavenumber is defined for a reference index of refraction $k = 2\pi n_r/\lambda$.

The equation for the field for $z > 0$ reduces to:

$$U(x,y,z>0) = -\int_{V'} \phi\left(\nabla^2 U + k^2 U\right) dV' - \int_{S'} \left(U \frac{\partial \phi}{\partial z}\right)_{z'=0} dS', \tag{16}$$

where S' is at the aperture plane $z' = 0$ and $\phi = G^+ - G^-$. If the index of refraction is changing, then the problem results in:

$$U(x,y,z>0) = -\int_{S'} \left(U \frac{\partial \phi}{\partial z}\right)_{z'=0} dS' + \int_{V'} \left(\phi k^2 \left(\left(\frac{n}{n_r}\right)^2 - 1\right) U\right) dV', \tag{17}$$

where the Green's functions for constant index of refraction has been retained. As can be seen, if the index of refraction is constant then (17) takes the more familiar form in cylindrical coordinates:

$$U(r,z) = \frac{-1}{2\pi} \frac{\partial}{\partial z} \int_0^{2\pi} \int_0^a U(r',0) \frac{e^{ik\sqrt{z^2+r^2+r'^2-2rr'\cos(\theta-\theta_0)}}}{\sqrt{z^2+r^2+r'^2-2rr'\cos(\theta-\theta_0)}} r' dr' d\theta, \tag{18}$$

where a is the aperture radius.

5.1.1. Aperture effects in the Fresnel region

For apertured beams, it is common to introduce the Fresnel number:

$$\mathcal{N}_F \propto \frac{a^2}{L\lambda}, \tag{19}$$

where here, a is a characteristic length of the aperture and L is the propagation length. For a square aperture, this becomes [9]:

$$\mathcal{N}_F = \frac{w_x w_y}{z\lambda}, \tag{20}$$

where $2w_x$ and $2w_y$ are the aperture widths in the x and y ordinates, respectively.

As will be shown in the next section, except for distances very close to the aperture, the paraxial approximation holds and the integral (18) can be compared to the results of solving (6). For the current computation, the aperture is not perfect but is modeled with a hyperbolic tangent with a slope of 200. Fig. 5 shows the agreement for a Fresnel number of 2 between the two methods. As one gets nearer the aperture, the oscillations in the solution become greater, but the parabolic method still gives a good agreement. This can be seen in the $\mathcal{N}_F = 10$ case in Fig. 6. The higher grid density in integral solution of (18) seen in Fig. 6 represents the required sampling density in the aperture plane of the solution. The disagreement near the edges in these figures is due to the oversimplified boundary conditions of $A = 0$ along the outer boundary of the parabolic method.

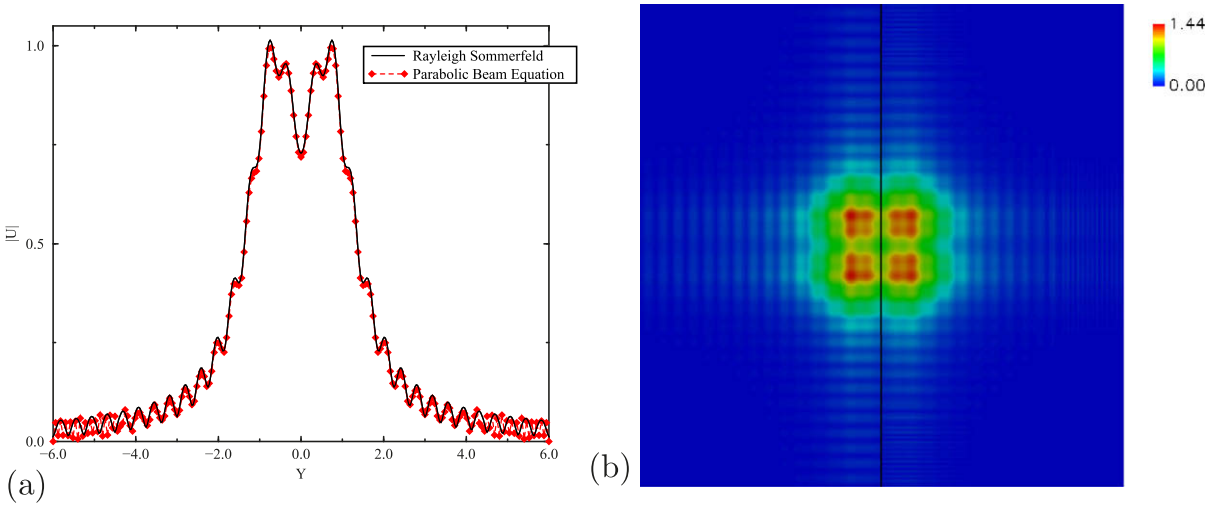

Fig. 5. Square aperture, $\mathcal{N}_F = 2$. (a) Magnitudes through the center of the aperture for the integral (18) and paraxial beam approximation (6) plotted on top of each other. (b) Magnitude of beam for both methods plotted side by side. Left: integral method. Right: parabolic beam solution.

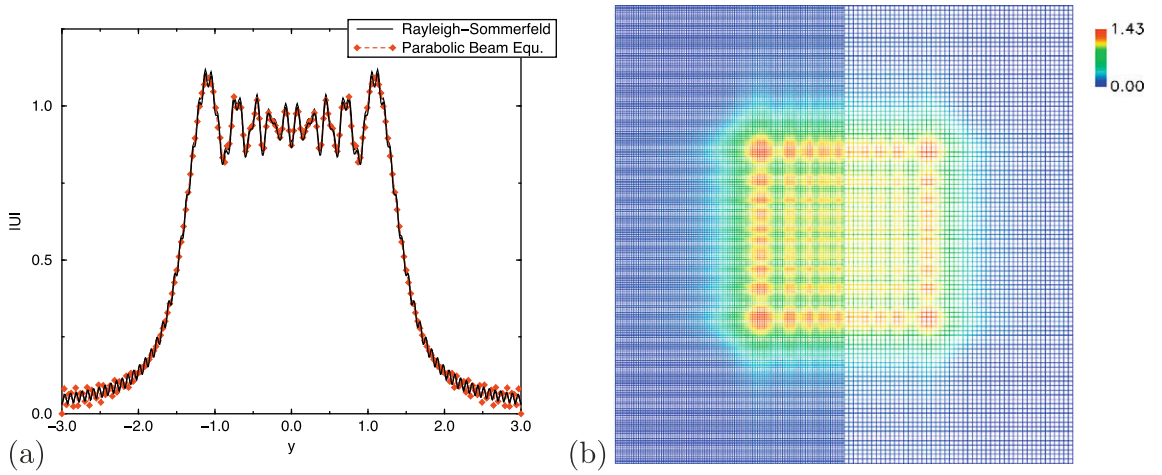

Fig. 6. Square aperture, $\mathcal{N}_F = 10$. (a) Magnitudes through the center of the aperture. [Solid line: integral Eq. (18). Symbols: paraxial beam approximation, Eq. (6).] (b) Magnitude of beam for both methods plotted side by side (every other gridline plotted). Left: integral method. Right: parabolic beam solution.

5.1.2. Near aperture, near-axis solution

Solving the Green's functions near the aperture can be numerically challenging for large wavenumbers due to the Green's function singularity. One method of solving the Rayleigh–Sommerfeld integrals was developed by Dubra and Ferrari [14] which gives the exact solution to the problem along the entire axis for circular apertures. In this method, the observation point is shifted to the (x', y') ordinates of the observation point as shown in Fig. 7. The key to their method is a translation of coordinates such that the reference point is located at $(0, 0, z)$. In this circumstance, Eq. (18) reduces to:

$$U(x,y,z) = \widetilde{U}(0,0,z) = \frac{z}{2\pi}\int_{\Sigma}\int U(r',\theta,0)\frac{e^{ik\sqrt{z^2+r'^2}}}{z^2+r'^2}\left(\frac{1}{\sqrt{z^2+r'^2}} - ik\right)r'dr'\,d\theta, \tag{21}$$

where $\widetilde{U}$ is simply U after having undergone a simple coordinate translation. Setting $U(r', \theta, 0) = U_0$ constant inside the aperture and making a change in variable

$$R^2 = r'^2 + z^2 \tag{22}$$

gives:

$$\widetilde{U}(0,0,z) = -\frac{zU_0}{2\pi}\int_{\theta_1}^{\theta_2}\frac{e^{ikR}}{R}\Big|_{R_{min}(\theta)}^{R_{max}(\theta)}d\theta. \tag{23}$$

If the observation point projects outside the aperture, then the integration needs to take place from the angles of the tangent lines from the origin to the aperture. If the observation point projects inside the aperture at $z = 0$ in the x–y plane, then the lower limit is just $R_{min}(\theta) = z$ and the equation reduces to:

$$\widetilde{U}(0,0,z) = U_0 e^{ikz} - \frac{zU_0}{2\pi}\int_0^{2\pi}\frac{e^{ikR_{max}(\theta)}}{R_{max}(\theta)}d\theta. \tag{24}$$

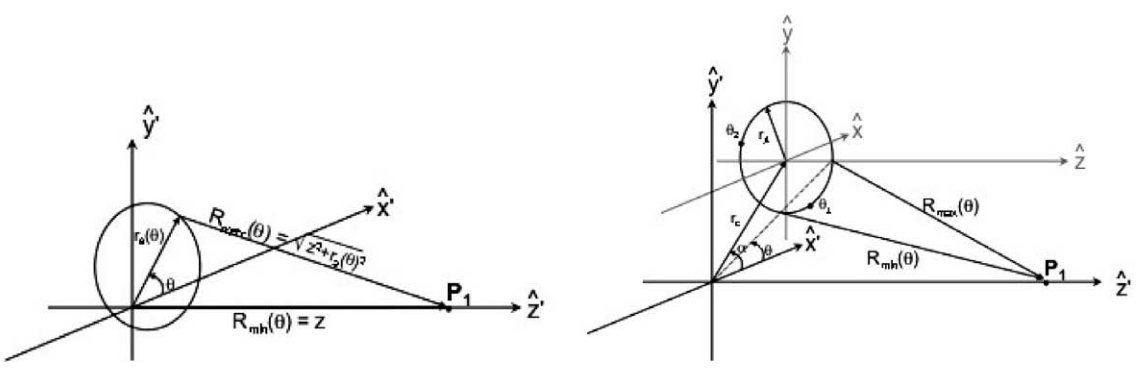

Fig. 7. Coordinates for Rayleigh–Sommerfeld integration of Dubra and Ferrari [14].

For solutions near the center line, the solution may also be approximated. Expanding R_{max} in terms of the distance r_c to the center of the aperture in the aperture plane:

$$R_{max} \approx \sqrt{a^2+z^2} + \frac{ar_c}{\sqrt{a^2+z^2}}\cos(\theta-\theta_c) + \left(\frac{\cos(2(\theta-\theta_c))}{2\sqrt{a^2+z^2}} - \frac{a^2\cos^2(\theta-\theta_c)}{2(a^2+z^2)^{\frac{3}{2}}}\right)r_c^2 + \mathcal{O}(r_c^3). \tag{25}$$

For $kr_c^2/\sqrt{a^2+z^2} \ll 1$, one may keep only the first two terms of R_{max} in the exponent [and just the first term in the denominator] of Eq. (24) to give:

$$U(r_c,z) \cong U_0\left(e^{ikz} - \frac{z}{\sqrt{a^2+z^2}}e^{ik\sqrt{a^2+z^2}}J_0\left(\frac{kar_c}{\sqrt{a^2+z^2}}\right)\right). \tag{26}$$

Since r_c is the distance near the aperture, this can be written as:

$$U(r,z) \cong U_0e^{ikz} - \frac{zU_0}{\sqrt{a^2+z^2}}J_0\left(\frac{kar}{\sqrt{a^2+z^2}}\right)e^{ik\sqrt{a^2+z^2}}. \tag{27}$$

For $r = 0$, this reduces to the exact analytical solution along the aperture axis [14].

As the observation plane approaches the aperture, a comparison of the exponential terms in (27) shows that the paraxial approximation for beam envelope breaks down. From a physical standpoint, the diffraction of the waves from the edge of the aperture interfere with the waves passing through the aperture. This might be especially important if one wished to include non-linear effects, such as thermal blooming into the model. The methodology of Dubra and Ferrari [14] was utilized to investigate these near aperture effects. The integration was implemented using systematic refinement (also known as composite rules [15]). The advantage to this implementation is that the solution can be systematically refined until the desired accuracy is achieved.

The numerical validation for the integration can be seen in comparison with the analytical value for the center line on a "top-hat" profile for a circular aperture as in Fig. 8. In this integration, the aperture is perfect (sharp). For the paraxial approximation, the aperture is again modeled with a hyperbolic tangent with slope of 200. To reduce the computational overhead, the non-dimensional wavenumber was reduced to 500 for these cases. The solution is computed at 1 radius away from the aperture. Fig. 9 shows that the agreement is in close agreement out near the edge, but the paraxial approximation misses the solution near the axis. Fig. 10(a) shows the solution near the axis along with the analytical correction of the last term of (27). As can also be seen in Fig. 10(b), the difference of the near-axis values has little effect on the far-field solution. This is likely due to the small amount of energy contained in this term.

One potential way to improve the accuracy of the parabolic equation near the aperture is to do a Born approximation for the equation where each refinement is another parabolic equation. Define:

$$A = A_0 + A_1 + A_2 + \cdots \tag{28}$$

For constant index of refraction this reduces to:

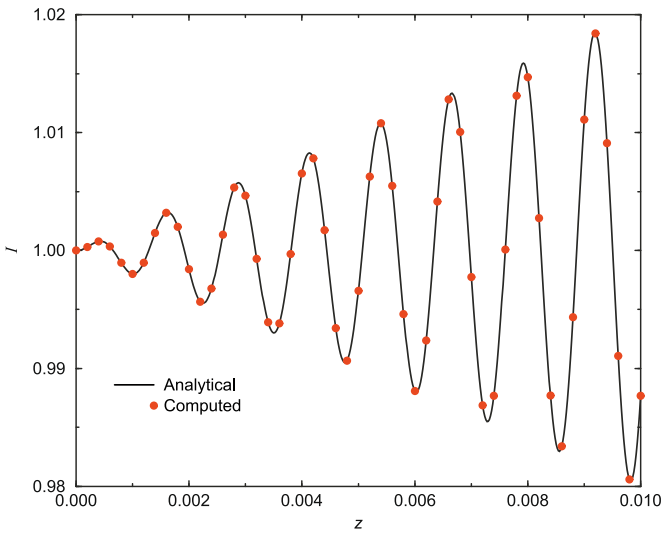

Fig. 8. Comparison of computed center line value with numerical integration with the analytical solution.

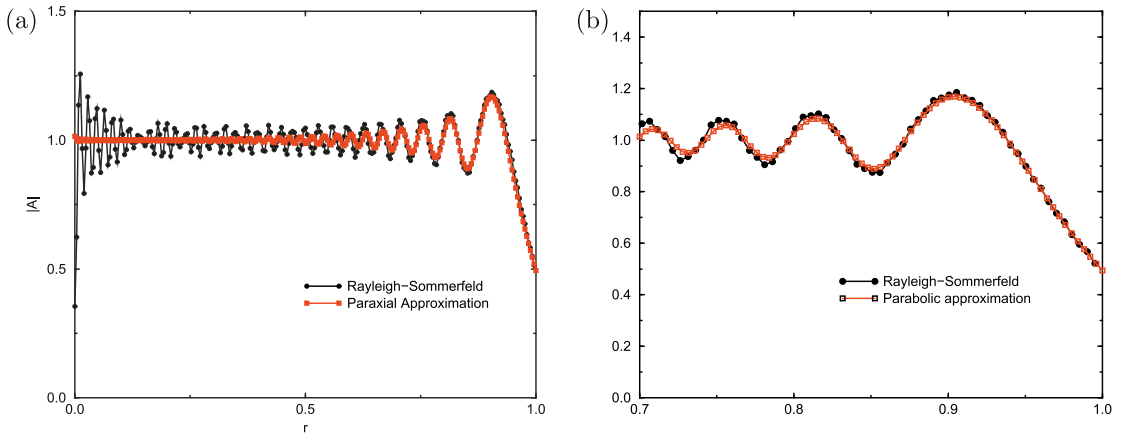

Fig. 9. Comparison of numerical integration with the paraxial solution.

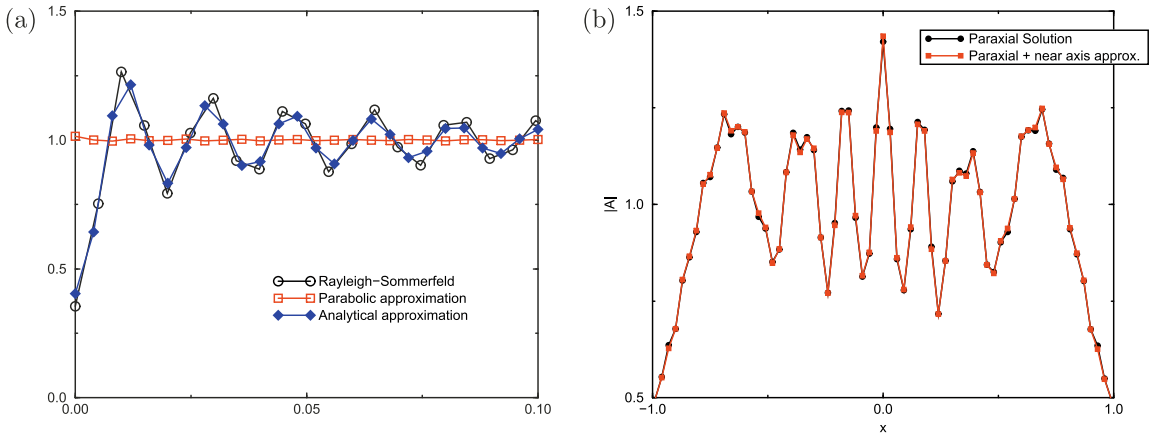

Fig. 10. Comparison of numerical integration near axis with the Rayleigh–Sommerfeld, paraxial beam solution and paraxial plus approximate analytical correction. (a) Comparison near axis. (b) Comparison of paraxial with paraxial plus analytic near-axis approximation.

$$2ik\frac{\partial A_0}{\partial z} \approx -\nabla_\perp^2 A_0, \tag{29}$$

$$2ik\frac{\partial A_1}{\partial z} \approx -\nabla_\perp^2 A_1 - \frac{\partial^2 A_0}{\partial z^2}, \tag{30}$$

...

To test this approach, the problem was further reduced to a two dimensional aperture, using the appropriate 2D Green's function:

$$G = \frac{i}{4}H_0^{(1)}(k\sqrt{(x-\xi)^2+z^2}). \tag{31}$$

The Hankel function is computed using the polynomial approximations given by Olver [16]. These approximations have an accuracy of better than 5×10^{-8}. The integrals were computed to at least one order of magnitude less that this. As can be seen in Fig. 11, this method may be used to improve the solution in this region. However, the combination of terms which behave like $e^{i\,k\,z}$ and $e^{ik\sqrt{a^2+z^2}}$ leads to harmonics which require a much smaller spatial step in integration.

5.2. Propagation through turbulence

5.2.1. Interpolation of density and resolution requirements

For a preliminary assessment of the resolution requirements of the flow field, the beams were propagated through compressible isotropic turbulence. This work used the 128^3 result from the high-order large-eddy simulation of Visbal and Rizzetta [17] using the Air Force Research Laboratory code FLD3DI [18]. The initial condition for this solution had an initial

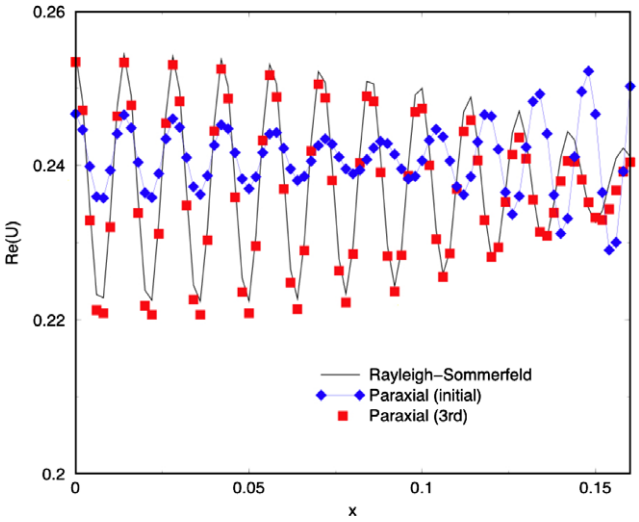

Fig. 11. Comparison of numerical integration near axis with the paraxial solution and approximate analytical solution.

turbulent Mach number of 0.4 (defined as the ratio of the RMS velocity to the mean speed of sound) [17]. The normalized RMS density fluctuation of this case was:

$$\langle \rho'^2 \rangle / \langle \rho \rangle^2 = 0.008$$

while the peak density variations were rather large ranging from approximately 0.6–1.6.

Two methods were used to transfer the density from the original grid to the aero-optics grid. The first method utilized a spectral interpolation procedure, whereby the density was transformed into Fourier space prior to being read into the code. This allows for great flexibility in gridding, as the spatial distribution can be calculated for any grid size as the solution advances. The density is first mapped into x and y by a 2D direct Fourier transform (DFT). While relatively computationally intensive, it is only done once at the beginning of the simulation. This leaves at each x, y ordinate a 1D Fourier series in z

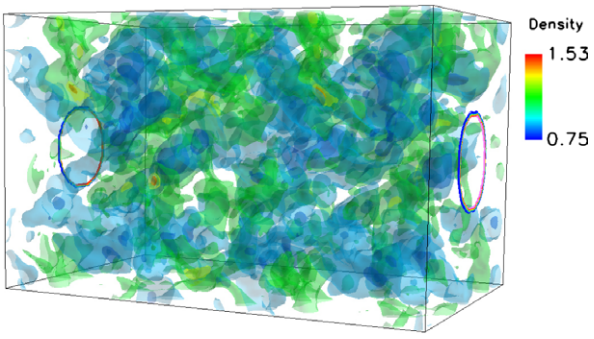

Fig. 12. Isotropic turbulence "box" $2\pi \times 2\pi$ in x and y and from 0 to 10 in z. (Tophat profile shown at $z = 0$ and $z = 12$.)

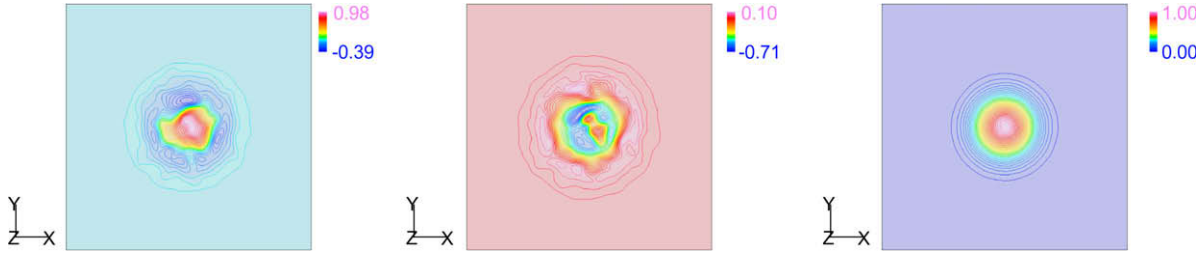

Fig. 13. Propagation of Gaussian beam to $z = 10$. Left: $\mathcal{R}e\{A\}$. Middle: $\mathcal{I}m\{A\}$. Right: $|A|$.

that can be summed for each location required by the Runge–Kutta integrator. It was for this reason that the standard RK4 was chosen, as aside from an initial calculation at $z = 0$, the density (and hence index of refraction) is only calculated twice during the four RK stages in each step.

The second method uses Lagrangian interpolation to map the density discrete onto the optical grid [19]:

$$\rho(x,y,z) = \sum_{j=\alpha_1}^{\beta_1} \sum_{k=\alpha_2}^{\beta_2} \sum_{\ell=\alpha_3}^{\beta_3} \left(\rho(x_j, y_k, z_\ell) \prod_{\substack{m=\alpha_1 \\ m \neq j}}^{\beta_1} \frac{x - x_m}{x_j - x_m} \prod_{\substack{n=\alpha_2 \\ n \neq k}}^{\beta_2} \frac{y - y_n}{y_k - y_n} \prod_{\substack{p=\alpha_3 \\ p \neq \ell}}^{\beta_3} \frac{z - z_p}{z_\ell - z_p} \right). \tag{32}$$

In the above equation, j, k, ℓ, m, n and p are all integers representing the index of the spatial variables on a Cartesian grid. As the grid for the parabolic equation in the transverse direction is kept fixed, the density is first interpolated onto that grid in the x and y directions. The code then interpolates the function in the z direction as necessary. In the code, the minimum stencil is two points bracketing the desired value. Thus at a minimum linear interpolation is performed. The stencil can be increased by one on both sides to increase the order of accuracy by two. The exception is near the boundaries where the interpolation becomes one-sided.

Since practical problems typically consist of a shear layer followed by relatively smooth flow, the density is further modulated by a hyperbolic tangent function: $(1 - \tanh[25(z - 10)])/2$. Some isosurfaces of the turbulence are shown in Fig. 12. While the real and imaginary parts of the change noticeably just after the turbulence, the magnitude appears unchanged by the turbulence as seen in Fig. 13. However, these distortions in the real an imaginary parts of the beam continue to affect the

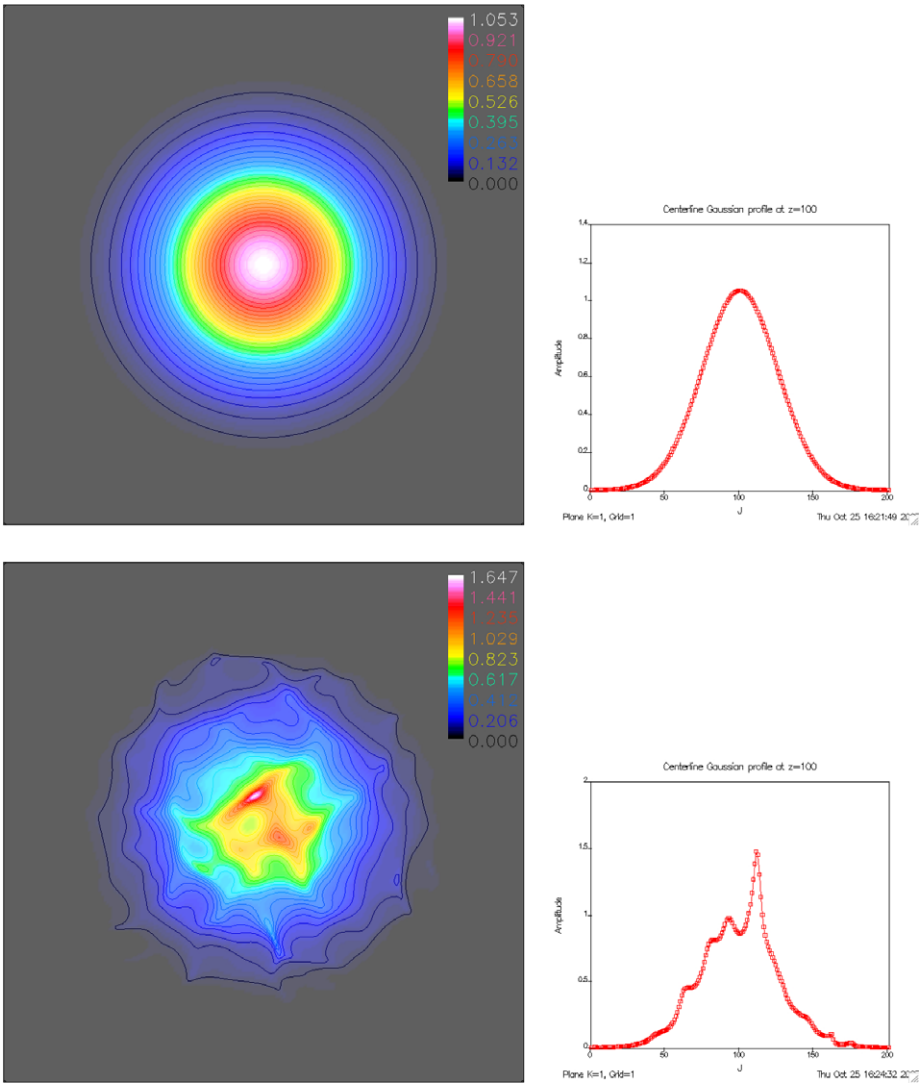

Fig. 14. Gaussian beam propagated to $z = 100$. Top: constant density. Bottom: isotropic turbulence to $z = 10$, followed by constant density.

beam while it propagates through the constant density region, and by $z = 100$, the bottom half of the Figs. 14 and 15 a noticeable distortion in both profiles.

To compare the effects of the Lagrangian interpolation, the optical path difference was calculated by integrating through the density field:

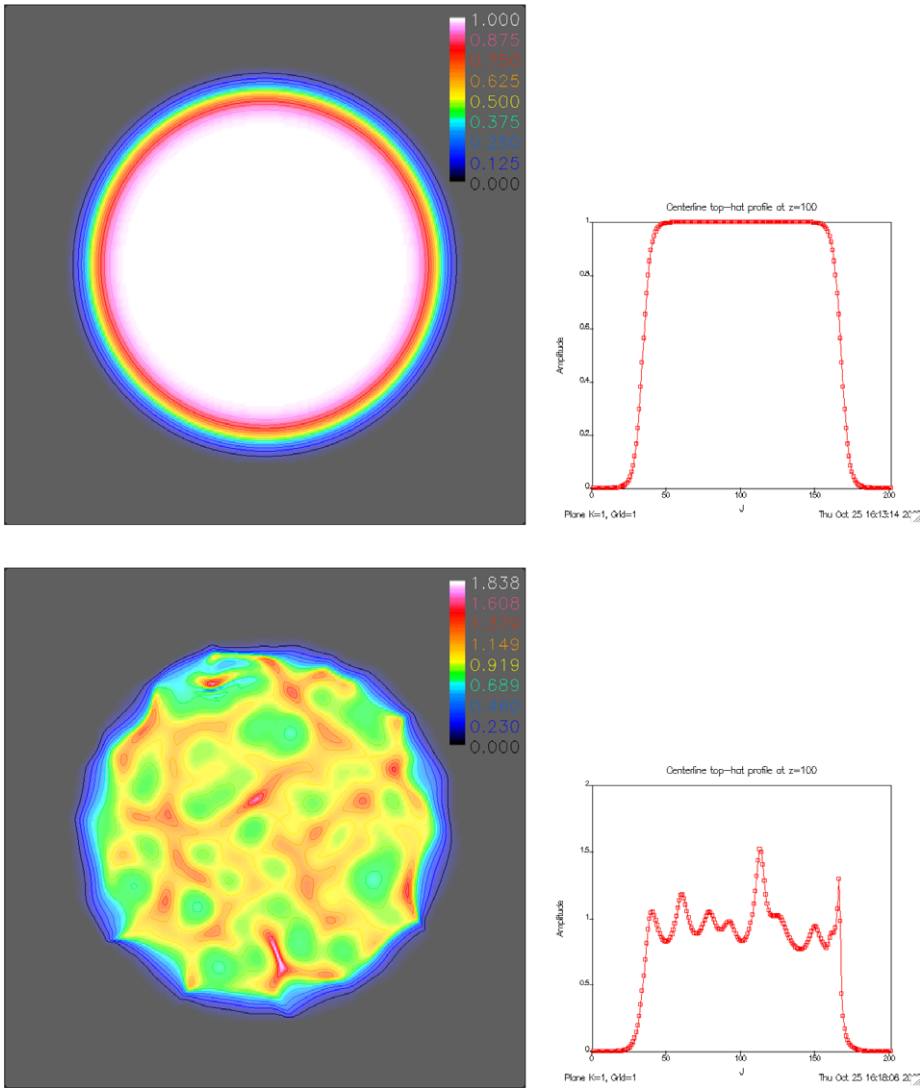

Fig. 15. Top-hat beam propagated to $z = 100$. Top: constant density. Bottom: isotropic turbulence to $z = 10$, followed by constant density.

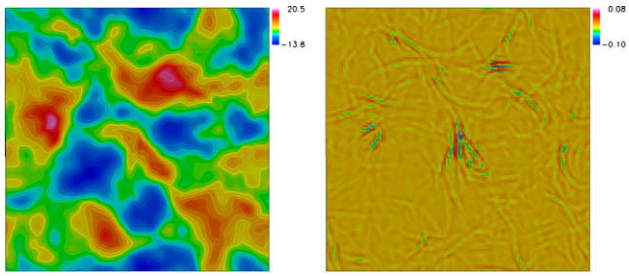

Fig. 16. OPD at $z = 10.4$. Left: 128 mode solution. Right: difference between 128 mode solution and 2-pt interpolation.

$$\mathrm{OPD} = \int_0^L (n - n_r)dz = \int_0^L K_{gd}(\rho - \rho_r)dz, \tag{33}$$

where ρ_r is the reference far-field density. The simulation was run to $z = 10.4$, just past the ramp down of the turbulent zone with a spatial step of 1/100th that of the spacing of the original turbulence grid. Both the background density grid and the aero-optics grid ranged from $\pm\pi$ in the x and y directions. The aero-optics grid had 221×221 points in the xy plane. The OPD is advanced with the same weights from the standard RK4 as the beam; which is equivalent to a Simpson's integration of the OPD. Lagrangian interpolation of even orders were compared to the reference density which was calculated using the full 128 mode spectral method; this being the highest resolution available based on the original data. The OPD and difference in the OPD as calculated using linear interpolation are given in Fig. 16. The results of the L_2 errors are given in the first row of Table 2.

The higher-order interpolations stop giving much improvement as the number of points is increased. This is mainly due to the one-sided interpolations at $z = 0$ and $x, y = \pm\pi$. To verify this, the background density was expanded using periodicity by 16 points in $-z$, $\pm x$ and $\pm y$ directions, so that no one-sided differences were used. The results as shown in the second row of Table 2. By reducing the slope of the hyperbolic tangent used to truncate the turbulent region from 25 to 5, the 34-pt interpolated solution is improved by a factor of about 2. The effect of the interpolation as the beam propagates in the z-direction is seen in Figs. 17 and 18.

5.2.2. Comparison of parabolic beam method and OPD

It is interesting to compare the phase difference from the beam equations with that calculated from the geometrical optics OPD. Examination of (4) and (57) [Appendix C] shows that for $\mathbf{k}\cdot\mathbf{s} = k\,z$ a phase difference can be calculated from the solution of the parabolic beam equation via:

Table 2
L2 error based on reference calculation of 128 modes.

2-pt	4-pt	6-pt	8-pt	10-pt	18-pt	34-pt
Lagrangian interpolation						
4.34×10^{-2}	7.17×10^{-3}	3.00×10^{-3}	1.77×10^{-3}	1.41×10^{-3}	2.37×10^{-3}	7.57×10^{-2}
Lagrangian interpolation w/ larger density domain						
4.34×10^{-2}	6.98×10^{-3}	2.85×10^{-3}	1.54×10^{-3}	9.54×10^{-4}	2.82×10^{-4}	1.38×10^{-4}

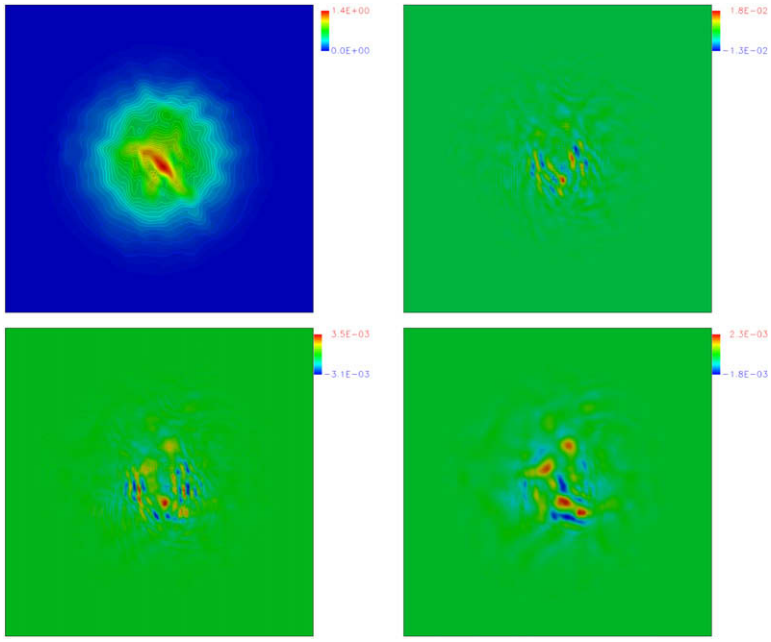

Fig. 17. Magnitude and error for beam propagated through turbulent region $z \in (0,10)$ at final location $z = 100$. Top left: magnitude shown for 128 mode case. Top right: difference between solutions using 2 interpolation points and the 128 mode case. Bottom left: difference using four interpolation points. Bottom right: difference using 10 interpolation points.

$$\delta\psi_b = -i\ln(A/A_r), \tag{34}$$

where A_r is the amplitude of the solution with the reference index of refraction n_r. As $\delta\psi_b$ is in general complex, the optical path difference from the beam solution may be determined from the real part:

$$\mathrm{OPD}_b = \frac{\lambda_{vac}}{2\pi}\mathcal{R}e\{\delta\psi_b\}. \tag{35}$$

While it is tempting to compare the OPD directly with the OPD_b, it is often safer to compare phase differences. The reason for this is that $\mathcal{R}e\{\delta\psi_b\}$ is constrained computationally by its definition in (34) to give the principle value between $(-\pi, \pi]$, while $\delta\psi_{go}$ in (60) [Appendix C] has no such constraint. Thus for comparison purposes, $\delta\psi_{go}$ should also be mapped to its principle value. There can still be a problem when $\mathcal{R}e\{\delta\psi_b\}$ and $\delta\psi_{go}$ lie close to but on different sides of the branch cut at $\pm\pi$. However, these jumps are easily detected and can be removed by the addition or subtraction of 2π as needed.

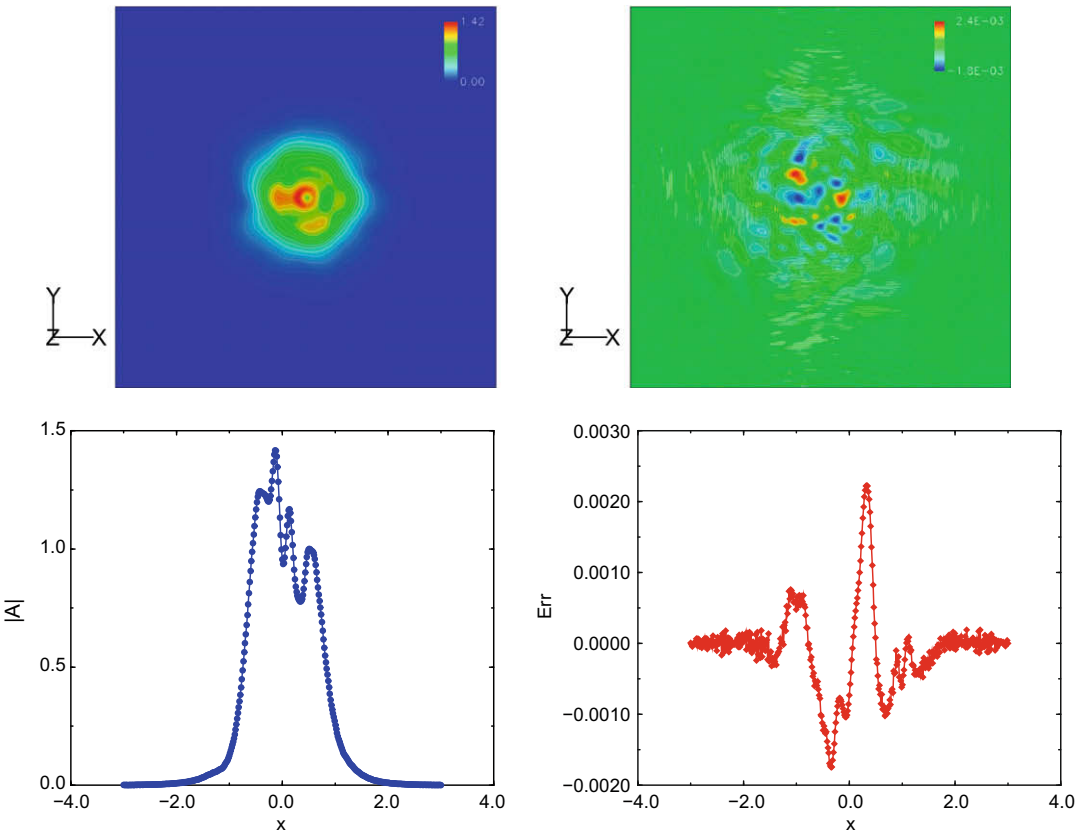

Fig. 18. Magnitude and error for beam propagated through turbulent region $z \in (0,10)$ at final location $z = 150$. Left: magnitude shown for two Lagrangian interpolation points. Right: difference between solutions using 2 and 18 interpolation points.

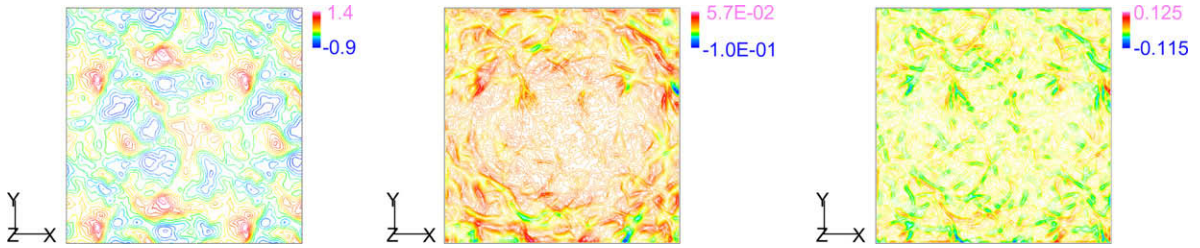

Fig. 19. Phase of Gaussian beam at $z = 10$. Left: real phase difference of Gaussian beam, $\mathcal{R}e\{\delta\psi_b\}$. Middle: difference of the real phase differences of Gaussian beam, $\Delta(\delta\psi)$. Right: imaginary part of the Gaussian beam phase difference, $\mathcal{I}m\{\delta\psi_b\}$.

To compare the parabolic beam method with OPD, the difference of the phase differences: $\Delta(\delta\psi) = \mathcal{R}e\{\delta\psi_b\} - \delta\psi_{go}$ is calculated. As seen in Fig. 19, the agreement between $\mathcal{R}e\{\delta\psi_b\}$ and $\delta\psi_{go}$ is $\lesssim 10\%$, especially in the main part of the beam, where it is under 5%. If a Gaussian beam is propagated through the turbulent zone out to a distance of $z = 100$ by (6), and compared with the solution from the Rayleigh–Sommerfeld equation with the analytical OPD, the difference is <2.5% as seen in Fig. 20.

For the apertured beam, there is another consideration as to whether aperturing the beam after the turbulent region is acceptable. On first look, it seems that the solution is noticeably different as shown in Fig. 21(a). Here the first two cases were the apertured Gaussian propagated via Eq. (6) to $z = 10$. In one case, the propagation was through the turbulent region, while in the other, it was propagated through free-space and OPD applied at $z = 10$. The agreement at $z = 100$ is quite good. Compared to this was the Gaussian apertured at $z = 10$ with the OPD applied. This result is noticeably different. However, if the last case is actually calculated at $z = 110$ rather than $z = 100$, the solution agrees with the previous two as seen in Fig. 21(b). This can be understood as shifting the aperture back to $z = 0$.

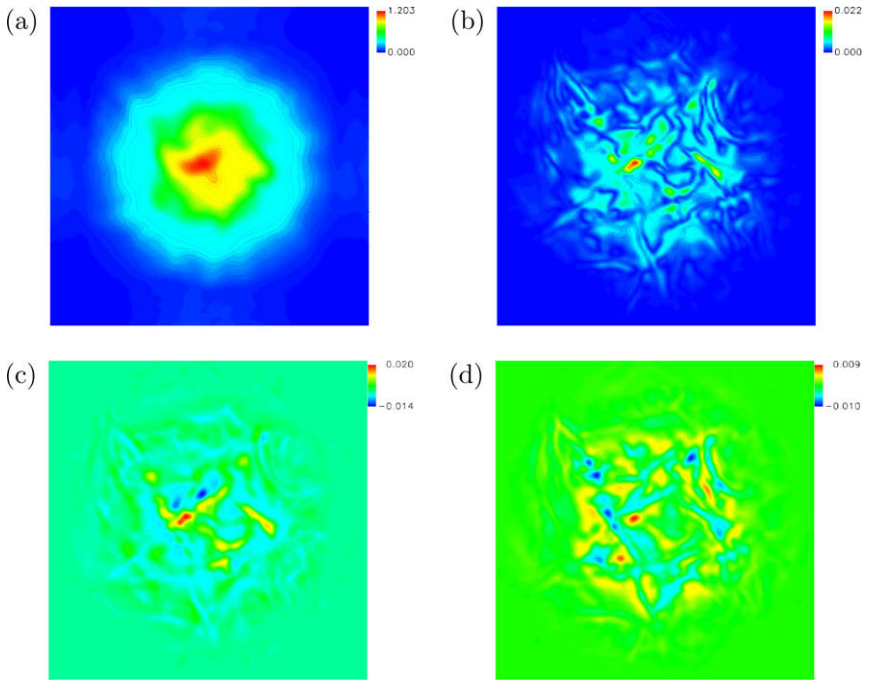

Fig. 20. Difference between parabolic approximation and OPD based calculation at $z = 100$. (a) Magnitude. (b) Magnitude difference. (c) Difference in real part of solution. (d) Difference in imaginary part of solution.

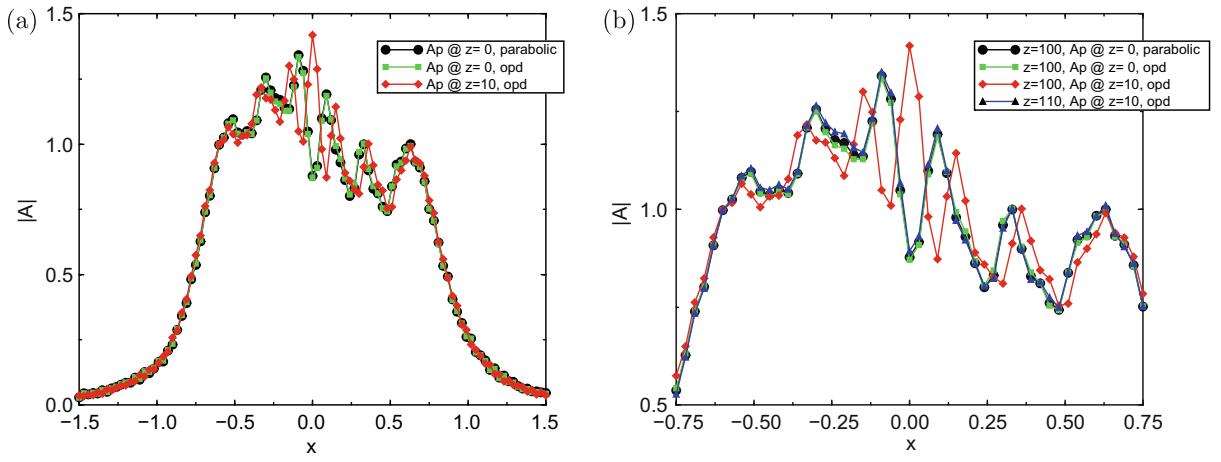

Fig. 21. Effect of aperture on location. (a) Comparison of aperturing with final distance $z = 100$. (b) Addition of solution for the Gaussian apertured at $z = 10$ with OPD applied and propagated to $z = 110$.

5.2.3. Propagation through a supersonic boundary layer

As an example of a more realistic flow, a Gaussian beam is propagated through a supersonic boundary layer with an incoming freestream Mach number of $Ma = 3.0$. The flow comes from a Large Eddy Simulation upstream of a compression ramp calculated by Rizzetta and Visbal [20]. The density is non-dimensionalized by the incoming freestream and achieves a high of 1.2 and low of 0.3 in the region where the beam is propagated. The Reynolds number based on the mean incoming boundary layer is $Re_{\delta_0} = 2.1 \times 10^{-4}$. Full details of the computation may be found in reference [20]. For the current computation, the $1/e$ beam radius was set equal to $r_0 = \delta_0$ and the beam center was set to be $5\delta_0$ upstream from the ramp to avoid effects of the separation at the shock location. The mean boundary layer at this location was roughly $\delta = 1$ mm in height. The transverse grid spacing was set to $\Delta x = \Delta y = \delta_0/45$. Fig. 22 shows the constant isosurface of density non-dimensionalized by the freestream of $\rho = 0.9$, along with the beam passing through the turbulence. The computation was run with wavelengths of 10.6 μm and 1.06 μm, representing a CO_2 and Nd-YAG lasers, respectively. As seen from Figs. 23 and 24, the longer wavelength shows a larger difference in the OPD when calculated by the two methods of Eqs. (33) and (35). This indicates that as

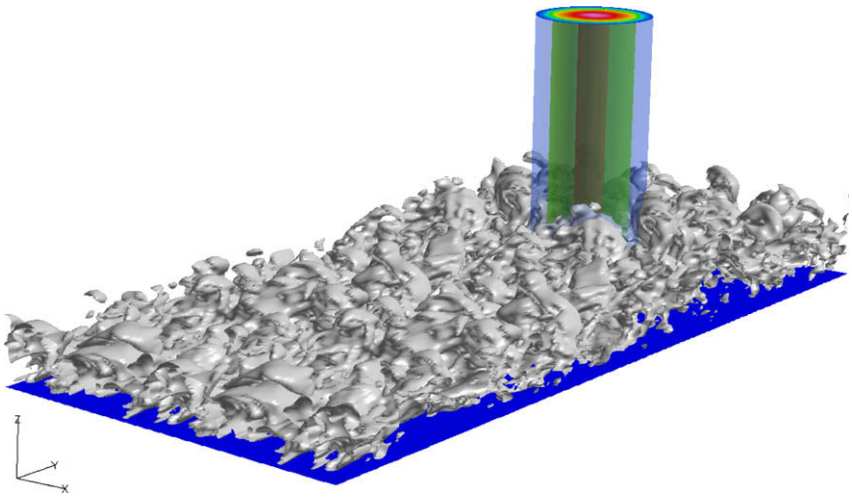

Fig. 22. Gaussian beam passing through a Mach 3 boundary layer. (Constant density isosurface of $\rho = 0.9$. Outer surface of beam is $r_o = \delta_0$.)

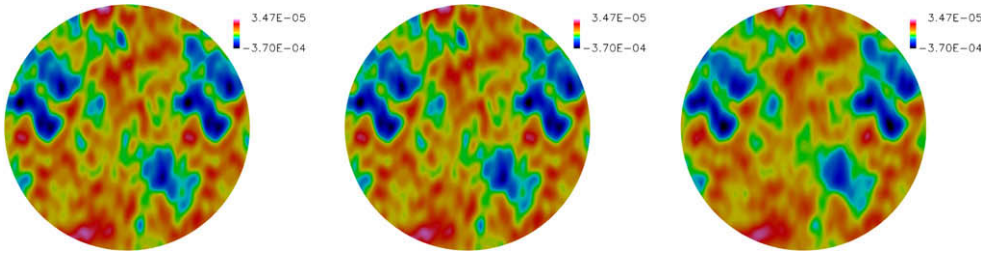

Fig. 23. Comparison of optical path difference. Left: OPD_b from the parabolic beam equation, $\lambda = 1.06$ μm. Middle: OPD integrated from Eq. (33). Right: OPD_b from the parabolic beam equation, $\lambda = 10.6$ μm.

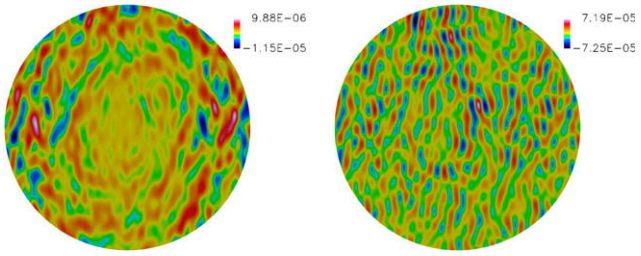

Fig. 24. Difference of OPD as calculated by the parabolic beam equation and Eq. (33). Left: $\lambda = 1.06$ μm. Right: $\lambda = 10.6$ μm.

the wavelength gets longer, the transverse terms of the phase become more important in the optical path (see Appendix C for details).

6. Conclusions

The parabolic beam method is shown to be an effective tool to investigate the interaction of laser beams with turbulent flow. The methodology is robust and can accurately model diffraction throughout the majority of the Fresnel region. The region very near the aperture are seen to be more difficult to resolve due to assumptions made in deriving the governing equation. The current study shows that the addition of a Born series approximation appears to be able to overcome the limitations from the paraxial approximation, but questions remain as to whether this might be the optimal solution due to resolution requirements. Another option might be to add in the analytical approximation for the near axis. While this will only correct the center of the beam, this is the region that gives the highest amplitude, and thus has the greatest potential impact for nonlinear effects.

The method has the ability to give quantitative information about the accuracy of traditional methods based on optical path differences, as well as being extendable to include more physical modeling. The results show that there appears to be little problem with aperturing after the turbulent zone and applying the OPD to the solution, if one takes care to make the appropriate adjustment to the target location. Perhaps a better viewpoint is that the OPD should be translated back to the aperture location before projecting to the far-field. The isotropic turbulence results affirm the view that the density does not need to be interpolated to as high an order of accuracy as is being used to solve the optics. The supersonic boundary layer results indicate that for long wavelength and high compressibility, neglecting of the transverse components in the traditional OPD may not be as accurate as for the shorter wavelengths.

Considering all of the unknowns in most aero-optical problems, the results clearly show that the traditional methods are more than suitable for the applications in which they are typically used. However, should one need to know the beam over some finite volume of space, the current method may be more desirable, due to the higher cost of calculating over volumes in the integral methods. The current method has shown that with the higher level of physical modeling, new insight can be gained on how the traditional methods behave and the limits of these methods may be more fully investigated. The parabolic equations can easily be used in conjunction with the traditional methods and gives the researcher another tool to use in simulating beam propagation.

Acknowledgments

The author thanks Miguel Visbal and Donald Rizzetta of the Air Force Research Laboratory (AFRL) for providing the turbulence data used for the study. The author would also like to thank the reviewer for their very helpful comments on this work. This project was sponsored by Arje Nachman of the Air Force Office of Scientific Research (AFOSR).

Appendix A. (2,4) Adaptive Runge–Kutta

The adaptive Runge–Kutta is formulated for an ode of the form:

$$dA/dz = f(z, A) \tag{36}$$

with

$$K_\sigma = \Delta z f\left(z^n + c_\sigma \Delta z, A^n + \sum_{\kappa=1}^{\sigma-1} a_{\sigma,\kappa} K_\kappa\right), \tag{37}$$

$$\overline{A}^{n+1} = A^n + \sum_{\sigma=1}^{4} \bar{b}_\sigma K_\sigma, \tag{38}$$

$$\widehat{A}^{n+1} = A^n + \sum_{\sigma=1}^{4} \hat{b}_\sigma K_\sigma. \tag{39}$$

The interpolation of the density for the index of refraction can be computationally intensive, especially in the cases where it is being calculated using direct Fourier transforms. Because of this, Kutta's standard 4th-order RK was chosen as the base solver as it only requires the index of refraction to be calculated twice (at locations $z^n + \Delta z/2$ and $z^n + \Delta z$) per marching step.

Fig. 25 gives the coefficients in standard Butcher Tableau notation.

The variables $\hat{b}_1 = \hat{b}_4 = \frac{1}{6}$ and $\hat{b}_2 = \hat{b}_3 = \frac{1}{3}$ are the coefficients for the standard 4th-order Runge–Kutta (RK4). Most adaptive Runge–Kuttas are formulated with an order pair (p − 1, p). Two of the most popular are the Fehlberg (4,5) pair [21] and the Dormand-Prince (4,5) pair [22]. However, these two methods require two more stages and more evaluations of the index of refraction. A (3,4) pair likewise requires at least five stages [21]. However, a (2,4) pair can be constructed for any 4th order RK with relative ease. This is because the only criterion is that the four weights $\bar{b}_1, \bar{b}_2, \bar{b}_3, \bar{b}_4$ must satisfy the first two order conditions, which in this case are:

0	0			
$\frac{1}{2}$	$\frac{1}{2}$	0		
$\frac{1}{2}$	0	$\frac{1}{2}$	0	
1	0	0	1	0
	$\bar{b}_1$	$\bar{b}_2$	$\bar{b}_3$	$\bar{b}_4$
	$\hat{b}_1$	$\hat{b}_2$	$\hat{b}_3$	$\hat{b}_4$

Fig. 25. Butcher table for adaptive Runge–Kutta.

$$\bar{b}_1 + \bar{b}_2 + \bar{b}_3 + \bar{b}_4 = 1, \tag{40}$$

$$\frac{\bar{b}_2 + \bar{b}_3}{2} + \bar{b}_4 = \frac{1}{2}. \tag{41}$$

In theory, the stability of the scheme should be the smaller of the two embedded RKs and an example is shown in Fig. 26. However, as the Runge–Kutta is to be advanced with the higher-order, the lower-order RK should have smaller stability region for possible eigenvalues of the problem in order to preclude a situation where the problem is slightly outside the stability region of the RK4 and diverges slowly enough that it does not trigger the adaptive step control.

The standard RK4 has a truncation error of order Δz^5, while the embedded RK has a truncation error:

$$\overline{A}^{n+1} = A(z^{n+1}) + \Delta z^3 \mathcal{L} + \mathcal{O}(\Delta z^4), \tag{42}$$

where $\mathcal{L} = \mathcal{L}\{f^n, \partial_z f^n, \partial_{zz} f^n, \partial_A f^n, \partial_{AA} f^n, \partial_{Az} f^n\}$ and $f^n \equiv f(z^n, A^n)$. Thus,

$$\mathcal{T}_e = \left|\widehat{A}^{n+1} - \overline{A}^{n+1}\right| \approx \left|\Delta z^3 \mathcal{L}\right| \tag{43}$$

represents a direct measure of the error per step at each point. However, depending on the shape of A, this might not capture the maximum error. To consider the maximum relative error, the following formulation may be used:

$$\mathcal{T}_n = \frac{\left|\widehat{A}^{n+1} - \overline{A}^{n+1}\right|}{|A^n| + \varepsilon_{sm}} \approx \left|\Delta z^3 \Lambda\right|, \tag{44}$$

where Λ is defined by the relation $\mathcal{L} = \Lambda A^n$ and ε_{sm} is a small value to prevent dividing by zero. While the relative error is generally preferred, it is possible for the solution to be diverging while keeping $\mathcal{T}_n$ bounded. Thus, the effective error estimate should be the maximum of the two values:

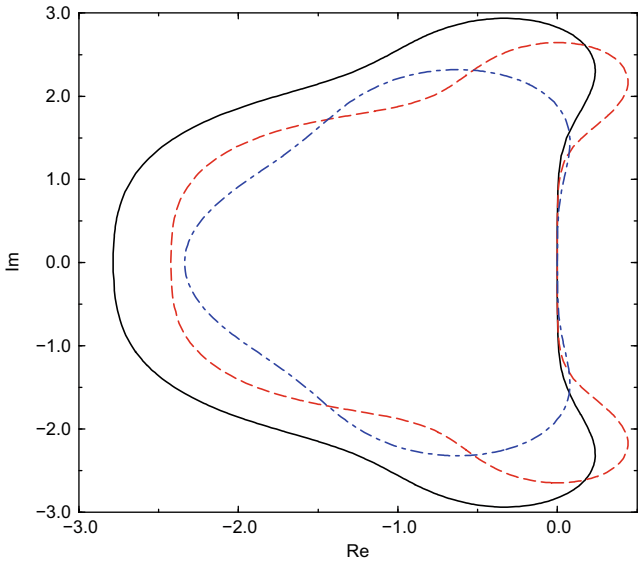

Fig. 26. Stability plot for the explicit Runge–Kutta. The solid line is standard Kutta's values, the dashed line is $\bar{b}_1 = \bar{b}_2 = \bar{b}_3 = \bar{b}_4 = 1/4$, and the dot-dash line is $\bar{b}_1 = \bar{b}_4 = 0,\ \bar{b}_2 = 1/4,\ \bar{b}_3 = 3/4$.

$$\mathcal{E} = \max(\mathcal{T}_e, \mathcal{T}_n) = |\Delta z^3| \max(|\mathcal{L}|, |\Lambda|). \tag{45}$$

This error estimate is desired to be kept below a local tolerance per unit step [15]:

$$\mathcal{E} \leqslant |\Delta z| \varepsilon_{tol}. \tag{46}$$

If one assumes that Λ (and hence $\mathcal{L}$) is approximately constant, then an ideal step ($\Delta\bar{z}$) based on the error estimate may be determined from:

$$|\Delta\bar{z}^3| \max(|\mathcal{L}|, |\Lambda|) = |\Delta\bar{z}| \varepsilon_{tol}. \tag{47}$$

By requiring that Δz change by factors of two, the condition may be written as:

$$\Delta\bar{z} = \frac{\Delta z}{2^p} \tag{48}$$

giving

$$\left| \frac{\mathcal{E}}{\Delta z \varepsilon_{tol}} \right| = 2^{3p-1} \tag{49}$$

or

$$p = \frac{1 + \log_2\left(\left|\frac{\mathcal{E}}{\Delta z \varepsilon_{tol}}\right|\right)}{3}. \tag{50}$$

If p is allowed to remain real, then Δz tends to change with every marching step. In the present work, p is usually rounded to the nearest integer.

The choice of which second order to use for the adaptive Runge–Kutta has little effect on the accuracy of the final solution as seen in Fig. 27. While the errors are very close here (and in some cases, the more accurate one is switched), there is a clear advantage of choosing $\mathbf{b}^T = \{1/4, 1/4, 1/4, 1/4\}$ over $\mathbf{b}^T = \{0, 1/4, 3/4, 0\}$. The former has a larger stability range and typically will solve the problem for a given tolerance in fewer steps. As can be seen in Fig. 28, the adaptive RK (aRK) tends to target the normalized rather than absolute error. As these errors are greatest very near to the boundary, it may indicate that the parameter ε_{sm} may not be sufficiently small enough. To assess the effect of the tolerances on the accuracy of the aRK, a Gaussian beam was propagated in constant density with the standard RK4 and fixed marching step-size. The grid was discretized with 201 × 201 points in x and y which corresponds to $\Delta x = \Delta y = 0.05$. The beam was marched 4000 steps to $z = 100$, giving a ratio of Δz to Δx of 0.5. The maximum error from the theoretical was $L_\infty = 5.76 \times 10^{-9}$ located at $(x, y) = (\pm 4.75, 0)$ and $(x,y) = (0, \pm 4.75)$. The L_1 norm was 3×10^{-10}. In the nearer domain bounded by $\pm\pi$, the errors drop to: $L_\infty = 9.3 \times 10^{-10}$ and $L_1 = 2.6 \times 10^{-12}$. A range of tolerances were tested against this RK4 solution and is shown in Table 3. Note that the code has been routinely run setting $\Delta z_0 = 1000$ and letting the aRK find its preferred step without any problems.

Appendix B. Details of verification methodology

To verify the implementation of the algorithm, the code was run with the index of refraction replaced with a complex parameter η.

This leads to Eq. (6) being:

$$\frac{\partial^2 A}{\partial r^2} + \frac{1}{r}\frac{\partial A}{\partial r} + \frac{1}{r^2}\frac{\partial^2 A}{\partial \theta^2} + 2ik\frac{\partial A}{\partial z} + \eta(r, \theta, z)A = 0. \tag{51}$$

For the methodology, a non-trivial analytic function is desired that will exercise all terms in the error expansion [12]. For the current case a trial solution was chosen to be:

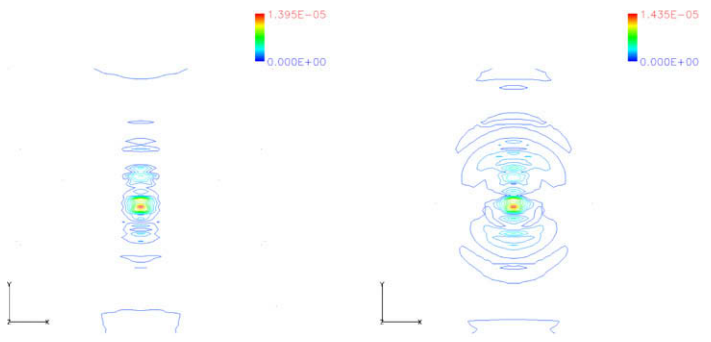

Fig. 27. Tolerance of adaptive RK set to 1.e−4. Left: b = (1/4,1/4,1/4,1/4). Right: b = (0,1/4,3/4,0).

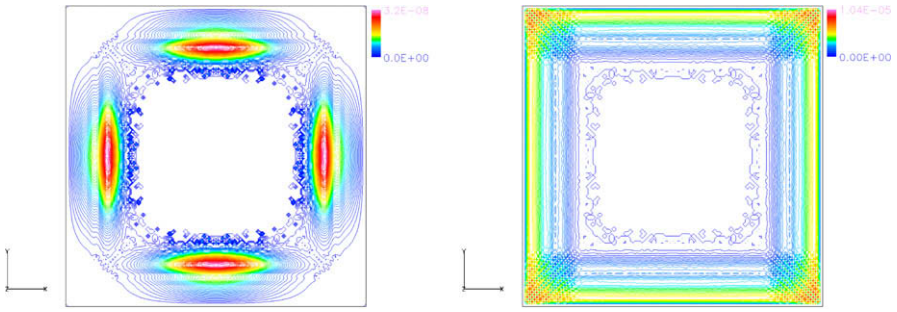

Fig. 28. Tolerance of adaptive RK set to 1.e−5 at $z = 100$. Left: $|A_{aRK} - A_{RK4,fine}|$. Right: $|A_{aRK} - A_{RK4,fine}|/|A_{RK4,fine}|$.

Table 3
Adaptive Runge–Kutta. Reference was run with $dz = 0.025$, 4000 iterations to convergence.

ε_{tol}	Δz_0	# Steps	min/max $\frac{\Delta z}{\Delta x}$	$\lvert A_{aRK} - A_{RK4,fine}\rvert$	$\frac{\lvert A_{aRK} - A_{RK4,fine}\rvert}{\lvert A_{RK4,fine}\rvert}$	Pwr (p)
10^{-5}	.05	141	4/32	1.4×10^{-12}	3.8×10^{-5}	Int
10^{-6}	.05	373	2/8	1.1×10^{-13}	2.0×10^{-7}	Int
10^{-7}	.05	1277	1/4	7.1×10^{-15}	1.0×10^{-7}	Int
10^{-6}	10	428	3.125/12.5	1.2×10^{-13}	4.4×10^{-7}	Int
10^{-6}	10	324	2.918/13.964	1.2×10^{-13}	7.7×10^{-7}	Real

$$A = \left(\frac{A_0}{1 + i\alpha z}\right) e^{-\frac{\alpha k r^2}{2(1+i\alpha z)} - \frac{\beta[z]\sin^2(\gamma r)\sin(\theta)}{r}}. \tag{52}$$

This leads to η being defined as:

$$\begin{aligned}\eta = {} & \frac{2ik\sin(\theta)\sin^2(\gamma r)\beta'[z]}{r} + \frac{(2\gamma(2\cos(\gamma r)\cos(2\theta)(\gamma r\cos(\gamma r) - \sin(\gamma r)) + \sin(2\gamma r)))\sin^2(\gamma r)\beta[z]^2}{2r^3} \\ & + \frac{((1 - 2\gamma^2 r^2)\cos(2\gamma r) - (1 + 2\gamma^2 r^2))\sin^2(\gamma r)\beta[z]^2}{2r^4} \\ & + \frac{\left(\alpha k r + (2(1 + i\alpha z)\gamma^2 - \alpha k)\cos(2\gamma r)r - \gamma\left(2\alpha k r^2 + (1 + i\alpha z)\right)\sin(2\gamma r)\right)\sin(\theta)\beta[z]}{r^2(1 + i\alpha z)},\end{aligned} \tag{53}$$

where γ and $\beta[z]$ are free parameters and α is a complex function of wavenumber and focal length [1]. The imaginary part of the index of refraction may be understood physically as modelling a linear absorption term. Note that η is bounded as:

$$\lim_{r\to 0}\eta = -\gamma^4\beta[z]^2, \tag{54}$$

$$\left|\lim_{r\to\infty}\eta\right| \leqslant \left|\frac{2\alpha\gamma k\beta[z]}{1 + i\alpha z}\right|. \tag{55}$$

For the current cases, the disturbance in (52) was run with the initial condition of (12), $\gamma = 15$ and the ramping function, $\beta[z]$ as:

$$\beta[z] = 0.1(0.5\tanh(d_1 z) + 0.75\tanh(d_2 z) - \tanh(z)). \tag{56}$$

The constants in $\beta[z]$ are $d_1 = 0.3622179832631045$ and $d_2 = 1.091854677824597$.

Appendix C. Rytov equation and OPD

The optical path difference (OPD) may be derived from the Helmholtz equation by considering changes in the phase of U. Writing the beam in terms of a scalar phase, $\psi(x,y,z)$, plus a propagating wave gives:

$$U(x,y,z) = a_0 e^{i\psi(x,y,z) + i\mathbf{k}\cdot\mathbf{s}}, \tag{57}$$

where $\mathbf{s}$ is distance in the direction of the propagation of the beam or ray. Again, making the paraxial approximation for ψ, Eq. (1) reduces to the Rytov equation [1]:

$$-2k\frac{\partial\psi}{\partial s} + i\nabla_\perp^2\psi - (\nabla_\perp\psi)^2 + k^2\left(\left(\frac{n}{n_r}\right)^2 - 1\right) = 0. \tag{58}$$

Letting ψ_r be the reference phase solution for Eq. (58) with $n = n_r$ and expanding $\psi = \psi_r + \delta\ \psi$, the change in phase due to density variations (neglecting terms of order $\delta\psi^2$) is:

$$-2k\frac{\partial\delta\psi}{\partial s} + i\nabla_\perp^2\delta\psi - 2(\nabla_\perp\psi_r)\cdot(\nabla_\perp\delta\psi) + k^2\left(\left(\frac{n}{n_r}\right)^2 - 1\right) \approx 0. \tag{59}$$

By setting $n = n_r + \delta n$ and neglecting the δn^2 and all transverse derivatives compared to the $k\partial_s$ term, Eq. (59) reduces to:

$$\delta\psi_{go} = k\int_0^L \left(\frac{n}{n_r} - 1\right)ds = \frac{2\pi}{\lambda_{vac}}\int_0^L (n - n_r)ds, \tag{60}$$

where $\delta\psi_{go}$ is recognized as the phase difference (using a geometrical optical approximation) and L is the length of the integration path. The optical path difference (OPD) based on the reference index of refraction n_r is:

$$\mathrm{OPD} = \int_0^L (n - n_r)ds. \tag{61}$$

If the deflection of the beam or ray is negligible, then the ds may be replaced with dz. Many researchers will take the reference index of refraction to be that of vacuum ($n_r = 1$).

References

[1] J.W. Strohbehn (Ed.), Laser beam propagation in the atmosphere, Topics in Applied Physics, vol. 25, Springer-Verlag, 1978.
[2] G.W. Sutton, Aero-optical foundations and applications, AIAA J. 23 (1985) 1525–1537.
[3] E.J. Jumper, E.J. Fitzgerald, Recent advances in aero-optics, Prog. Aerospace Sci. 37 (2001) 299–339.
[4] P.B. Ulrich, Numerical methods in high power laser propagation, in: Optical Propagation in the Atmosphere, AGARD CP-183, 1976, pp. 31/1–31/19.
[5] K.H. Craig, Propagation modelling in the troposphere: parabolic equation model, Electron. Lett. 24 (18) (1988) 1136–1139.
[6] P. Sprangle, J.R. Peñano, B. Hafizi, Propagation of intense short laser pulses in the atmosphere, Phys. Rev. E 66 (4) (2002) 046418.
[7] A. Mani, M. Wang, P. Moin, Resolution requirements for aero-optical simulations, J. Comput. Phys. 227 (2008) 9008–9020.
[8] J.D. Jackson, Classical Electrodynamics, second ed., McGraw-Hill Book Company, 1990.
[9] J.W. Goodman, Introduction to Fourier Optics, third ed., Roberts & Company, 2004.
[10] L.C. Andrews, R.L. Phillips, Laser Beam Propagation Through Random Media, second ed., SPIE Press, 2005.
[11] S.K. Lele, Compact finite difference schemes with spectral-like resolution, J. Comput. Phys. 103 (1992) 16–42.
[12] P.J. Roache, Code verification by the method of manufactured solutions, J. Fluid Eng. 24 (2002) 4–10.
[13] G. Arfkin, Mathematical Methods for Physicists, third ed., Academic Press, 1985.
[14] A. Dubra, J. Ferrari, Diffracted field by an arbitrary aperture, Am. J. Phys. 67 (1) (1999) 87–92.
[15] S.D. Conte, C. de Boor, Elementary Numerical Analysis, third ed., McGraw-Hill, 1985.
[16] F.J.W. Olver, Bessel functions of integer order, in: M. Abramowitz, I.A. Stegun (Eds.), Handbook of Mathematical Functions, Dover, 1972, pp. 369–370.
[17] M.R. Visbal, D.P. Rizzetta, Large-eddy simulation on curvilinear grids using compact differencing and filtering schemes, Trans. ASME 124 (2002) 836–847.
[18] D. Gaitonde, M. Visbal, High-order schemes for Navier–Stokes equations: algorithm and implementation into FDL3DI, Tech. Rep. AFRL-VA-WP-TR-1998-3060, Air Force Research Labs, 1998.
[19] C.R. Wylie, L.C. Barrett, Advanced Engineering Mathematics, McGraw-Hill, 1982.
[20] D.P. Rizzetta, M.R. Visbal, Application of large-eddy simulation to supersonic compression ramps, AIAA J. 40 (8) (2002) 1574–1581.
[21] E. Fehlberg, Low-order classical Runge–Kutta formulas with stepsize control and their application to some heat transfer problems, Tech. Rep. TR R-315, NASA, 1969.
[22] J.R. Dormand, P.J. Prince, A family of embedded Runge–Kutta formulae, J. Comput. Appl. Math. 6 (1) (1980) 19–26.